

TOOLS AND RESOURCES

GIANI – open-source software for automated analysis of 3D microscopy images

David J. Barry^{1,*}, Claudia Gerri^{2,3}, Donald M. Bell¹, Rocco D’Antuono¹ and Kathy K. Niakan^{2,4}

ABSTRACT

The study of cellular and developmental processes in physiologically relevant three-dimensional (3D) systems facilitates an understanding of mechanisms underlying cell fate, disease and injury. While cutting-edge microscopy technologies permit the routine acquisition of 3D datasets, there is currently a limited number of open-source software packages to analyse such images. Here, we describe General Image Analysis of Nuclei-based Images (GIANI; <https://djpbarry.github.io/Giani/>), new software for the analysis of 3D images. The design primarily facilitates segmentation of nuclei and cells, followed by quantification of morphology and protein expression. GIANI enables routine and reproducible batch-processing of large numbers of images, and comes with scripting and command line tools. We demonstrate the utility of GIANI by quantifying cell morphology and protein expression in confocal images of mouse early embryos and by segmenting nuclei from light-sheet microscopy images of the flour beetle embryo. We also validate the performance of the software using simulated data. More generally, we anticipate that GIANI will be a useful tool for researchers in a variety of biomedical fields.

KEY WORDS: 3D, FIJI, Image analysis, Open source

INTRODUCTION

The ability to routinely acquire multi-dimensional datasets with modern microscopy techniques is transforming, among other fields, cell biology, developmental biology and cancer research. There has long been an acceptance that two-dimensional (2D) cell cultures might not accurately recreate behaviours found in complex three-dimensional (3D) *in vivo* environments (Duval et al., 2017). Commonly used 3D culture formats include, but are not limited to, populations of single cells in organotypic matrices, spheroid models, tissue sections or whole embryos and organisms.

However, the development of software for the quantitative analysis of such data has not kept pace with imaging advances, and

there is now a pressing need for automated solutions (Meijering et al., 2016). Manual annotation of such data is not feasible in a reasonable time frame. Commercial packages, such as Imaris (Bitplane) and Vison4D (Arivis) provide excellent visualisation functionality and are also equipped with analysis tools. However, licences for such software are expensive and they also rely on proprietary file formats. Furthermore, the closed-source nature of such software prevents detailed interrogation of specific calculations and processes.

There are numerous excellent, freely available bioimage analysis tools in the open source domain. However, their support for 3D analysis is often limited – for example, several CellProfiler (Lamprecht et al., 2007) modules are not yet compatible with 3D images. In cases where 3D datasets are supported, analyses can be challenging to execute for novice users, potentially requiring a complex combination of commands from multiple plugins [e.g. FIJI (Schindelin et al., 2012) and Icy (de Chaumont et al., 2012)]. This can lead to undesirable compromises being made, such as 2D slices from a 3D volume being analysed individually, blinding the analysis to information in adjacent slices. Alternatively, 3D data might be compressed into 2D via projection, which, consequently, artificially reduces distances between objects and can lead to spurious results. A number of very useful open-source MATLAB (MathWorks, Cambridge, UK)-based tools have also been implemented, most notably MINS, which has been effectively used to analyse embryo datasets (Lou et al., 2014) and LOBSTER (Tosi et al., 2020). However, these require the purchase of a MATLAB licence.

We have therefore developed General Image Analysis of Nuclei-based Images (GIANI; <https://djpbarry.github.io/Giani/>), a generally applicable open source tool, implemented as a plugin for the widely-used image analysis platform FIJI. With an emphasis on detection and segmentation of cells in 3D microscopy images, GIANI has been implemented specifically with batch-processing in mind. Although an understanding of fundamental concepts of bioimage analysis is beneficial, GIANI’s user interface has been implemented in a wizard format to facilitate use by non-specialists (Fig. 1) and is fully documented (<https://github.com/djpbarry/Giani/wiki>). Analysis protocols may be reproduced by loading a single parameter file.


The utility of GIANI is illustrated here using three examples. In the first, we generated a series of simulated datasets to evaluate the accuracy of segmentations produced by GIANI using known ‘ground truths’. In the second proof-of-concept, we use a series of mouse preimplantation embryo datasets, and demonstrate the ability of GIANI to detect variations in morphology and protein expression in different experimental conditions. Finally, to show that GIANI can also be used on much larger datasets, we present segmentations of nuclei from light-sheet microscopy images of the flour beetle embryo. It should be noted that GIANI can be used to analyse 3D images from a range of cellular and developmental contexts, and we

¹Crick Advanced Light Microscopy, Francis Crick Institute, London NW1 1ST, UK.

²Human Embryo and Stem Cell Laboratory, Francis Crick Institute, London NW1 1ST, UK.

³Max Planck Institute of Molecular Cell Biology and Genetics, Pfotenhauerstrasse 108, 01307 Dresden, Germany. ⁴The Centre for Trophoblast Research, Department of Physiology, Development and Neuroscience, University of Cambridge, Cambridge CB2 3EG, UK.

*Author for correspondence (david.barry@crick.ac.uk)

 D.J.B., 0000-0003-2763-5244; C.G., 0000-0002-9046-3820; D.M.B., 0000-0002-3788-1580; R.D., 0000-0003-0180-6500; K.K.N., 0000-0003-1646-4734

This is an Open Access article distributed under the terms of the Creative Commons Attribution License (<https://creativecommons.org/licenses/by/4.0/>), which permits unrestricted use, distribution and reproduction in any medium provided that the original work is properly attributed.

Handling Editor: Jennifer Lippincott-Schwartz
Received 26 October 2021; Accepted 20 April 2022

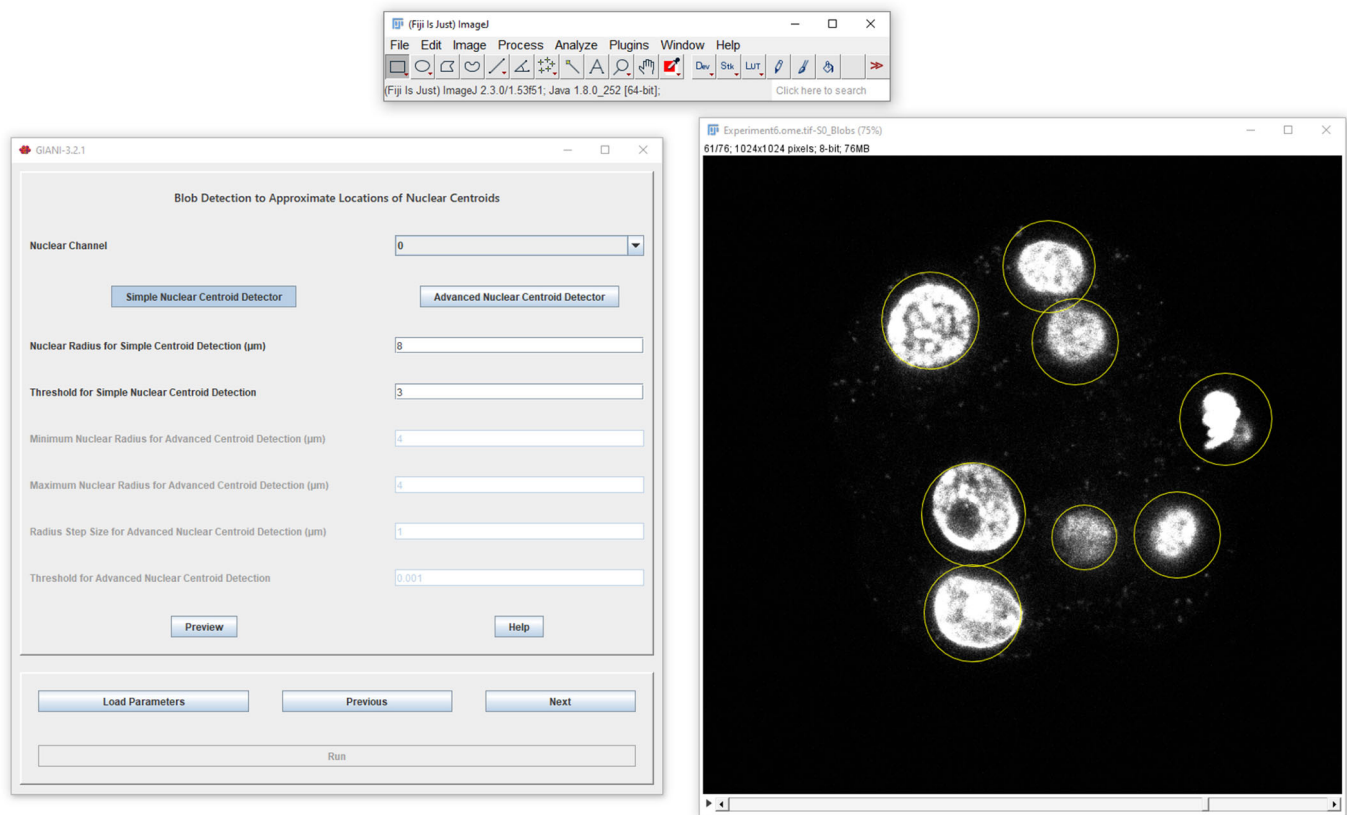


Fig. 1. Illustration of the GIANI graphical user interface. The GIANI parameter-setting wizard is shown on the left, with the preview result of this particular processing step (nuclear centre detection) shown on the right.

anticipate that it will be a useful tool to automate quantification of a wide variety of complex imaging data.

RESULTS

Software implementation

GIANI was written using Java 8 as a plug-in for FIJI (Schindelin et al., 2012), making extensive use of the underlying FIJI and ImageJ (Schneider et al., 2012) libraries. A number of other open-source projects were leveraged. Reading of image data is facilitated by interfacing to Bio-Formats (Linkert et al., 2010), making GIANI compatible with a wide range of file formats (<https://docs.openmicroscopy.org/bio-formats/6.7.0/supported-formats.html>). Detection of nuclear blobs makes use of either TrackMate's spot detector (Tinevez et al., 2017) or FeatureJ (<https://imagescience.org/meijering/software/featurej>). Segmentation of cells and nuclei takes advantage of the marker-controlled watershed functionality in MorphoLibJ (Legland et al., 2016) and 3D Image Suite (Ollion et al., 2013). The browsing of results is based upon the 3D region of interest (ROI) manager from 3D Image Suite. Complete source code, documentation and test data are available online (<https://djpbarry.github.io/Giani>).

The design philosophy behind GIANI is inspired by CellProfiler. It is assumed that the user wishes to detect 'primary objects' of some sort (typically cell nuclei), followed by the subsequent segmentation of 'secondary objects' (typically cells) and then wishes to measure either the morphology of, or the expression of a fluorescent signal within, these objects. The principal difference in the case of GIANI is that, in order to facilitate ease of use, the order of steps in the pipeline is fixed, although some flexibility is present where necessary (Fig. 2).

File formats

GIANI can accept as input any images that are readable by Bio-Formats (Linkert et al., 2010), which, at the time of writing, can read almost 160 different formats. It is expected that this data will be 3D in nature, containing any number of different channels. As a minimum requirement, in order to facilitate accurate segmentation, these channels must contain some form of marker for both nuclei and cells. The nuclear marker must be a volume marker, whereas the cell marker can be either membrane localised or volumetric in nature, although the former is preferred for more accurate segmentation. In the example pipeline illustrated in Fig. 2, a nuclear volume marker (DAPI) and cell membrane marker (E-cadherin) are used.

Detection of nuclear centres

The nuclear channel is first subjected to one of two forms of blob detection to estimate the centre of each nucleus (Fig. 2B). The first option is Laplacian of Gaussian (LoG) blob detection, which involves the application of an LoG filter to the image and then identifying local extrema (Fig. 2B, left panels). This is implemented in GIANI by using the spot detector of TrackMate (Tinevez et al., 2017), which is based on LoG detection. The advantage of this approach is that it is relatively fast and generic. The disadvantage is it assumes the objects to be detected are approximately Gaussian in nature, so will likely perform poorly for irregularly shaped nuclei.

For this reason, a second option is given for nuclear centre detection, based on the eigenvalues Hessian matrix of the image (Fig. 2B, right panels) – this is similar to the approach used for nuclear detection in MINS (Lou et al., 2014). The Hessian is a square matrix of second-order partial derivatives describing the

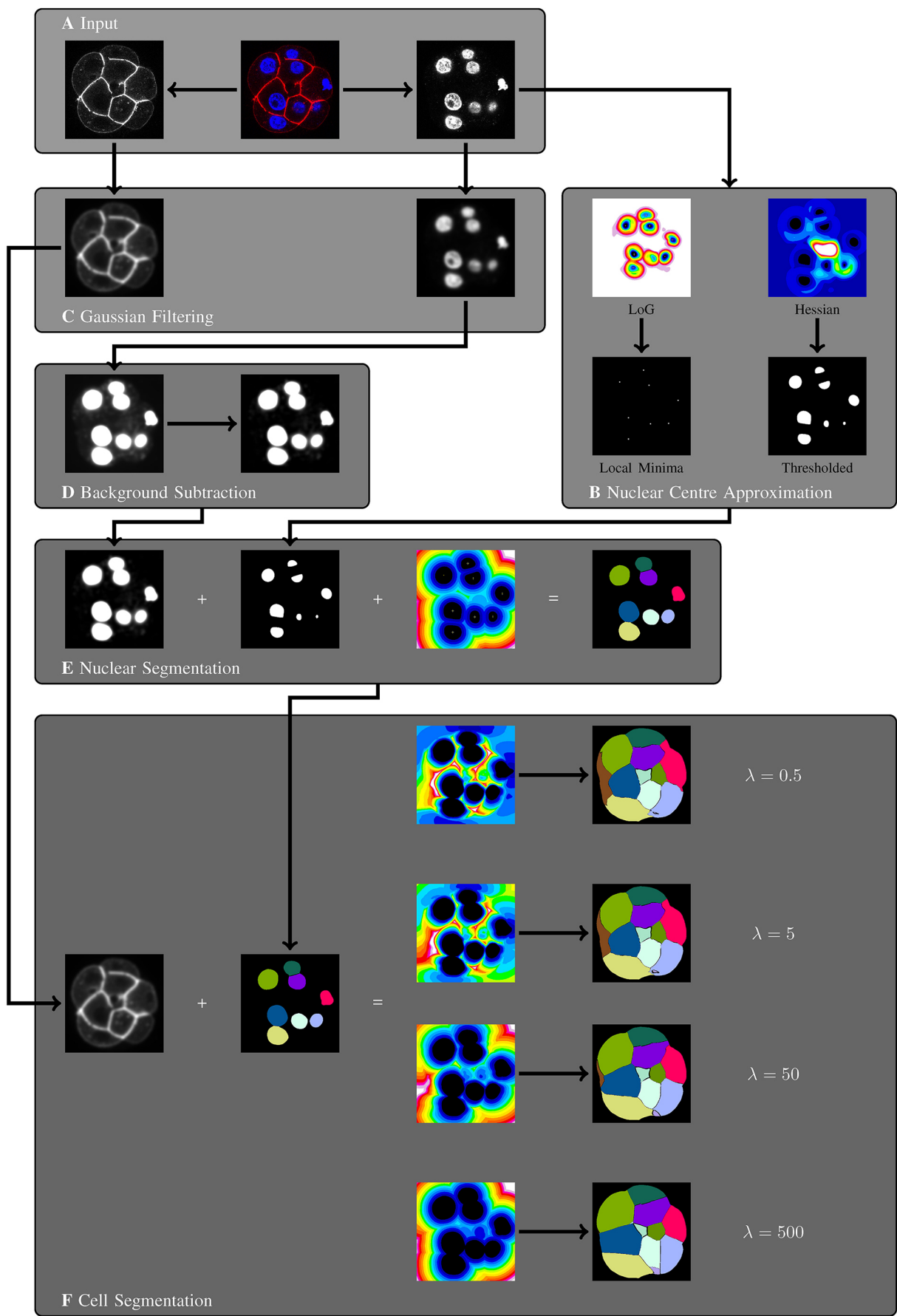


Fig. 2. See next page for legend.

Fig. 2. Overview of the algorithms underpinning GIANI. All images represent a single slice of a 3D stack and are for illustrative purposes only. (A) An example dataset, consisting of a mouse embryo showing DAPI (blue) and E-cadherin (red). GIANI can accept as input any image data that is readable by Bio-Formats (Linkert et al., 2010). (B) Nuclear centres are first approximated using one of two blob detectors – Laplacian of Gaussian (left) or Hessian (right). (C) Gaussian filtering is used to suppress noise in the channels used for nuclear and cell segmentation. (D) The nuclear channel is then subjected to top-hat filtering to remove background; contrast has been increased to illustrate the effect of the filter. (E) Nuclear segmentation is achieved using a marker-controlled watershed approach, with the background-subtracted image from D serving as the input and approximated centres from B serving as the seeds. (F) Cell segmentation is achieved using the same marker-controlled watershed approach, with the filtered image from C serving as the input and nuclei segmentations from E serving as the seeds.

local curvature in the image. For a detailed explanation on how Hessian eigenvalues can be used to detect blobs in images, see Cautun et al. (2012). This is implemented in GIANI by using FeatureJ, a sub-component of the ImageScience plugin (<https://imagescience.org/meijering/software/featurej>). This approach has the advantage of being capable of detecting ‘blobs’ of any shape, such as irregularly shaped nuclei. The main disadvantage is that it is much more computationally demanding than the simpler LoG detector, so will take longer to run.

Suppression of noise and background

Prior to full segmentation of nuclei, Gaussian filtering is employed to smooth any noise that may have been present in the input image (Fig. 2C). To both enhance the nuclei and homogenise the image background, the output of the Gaussian filtering operation is input into a top-hat filter (Fig. 2D), implemented using MorphoLibJ (Legland et al., 2016). Top-hat filtering can be computationally expensive for large datasets, so GIANI includes an option to downsize datasets by a specified factor prior to this step – the dataset is then restored to its original size post-filtering.

Segmentation of nuclei

Nuclei are fully segmented using a marker-controlled watershed approach (Fig. 2E). GIANI uses MorphoLibJ to achieve this, with the previously detected nuclear centres serving as seeds and the Euclidean Distance Transform of the nuclear centre mask, calculated using the 3D ImageJ Suite (Ollion et al., 2013), serving as the image to be flooded. In addition, the top-hat filtered nuclei channel is thresholded (using one of FIJI’s in-built thresholding algorithms, specified by the user) to act as a mask, restricting the overall extent of the segmentation.

Segmentation of cells

Cells are segmented using the same marker-controlled watershed approach (Fig. 2F), with the previously segmented nuclei serving as seeds and the distance transform of the nuclei serving as the image to be flooded. The Gaussian-filtered cell channel (Fig. 2C) is thresholded to act as a mask in this case. The nature of the distance transform used is dependent on whether a membrane marker or volume marker is used to identify the cells. In the case of a volume marker, a standard Euclidean Distance Transform is used. In the case of a membrane marker, a modified distance transform is used, similar to that described by Jones et al. (2005), where the distance between adjacent voxels, d , is calculated based on a Riemannian metric defined in terms of the image I and a regularisation parameter, λ :

$$d = \frac{\nabla I + \lambda}{1 + \lambda}. \quad (1)$$

It can be seen that as λ tends to infinity, d tends towards the Euclidean distance.

Analysis of simulated embryos

To first validate the performance of GIANI, we generated a series of 189 ‘simulated embryos’ exhibiting different levels of signal-to-noise ratio and cell density (Fig. 3A). Simulated data has the significant advantage of having a known ‘ground truth’ (Fig. 3B). That is, because the images are generated artificially, we know what the ‘correct’ segmentation should look like. This permits us to compare the segmentation results generated with any piece of analysis software with the known ‘true’ values.

Cell count errors generally increased with increased cell density and decreasing signal-to-noise ratio (Fig. 3C,F). However, this error was equal to 1 or less in 82.0% of embryos analysed using GIANI’s basic nuclear detection and 98.9% when using advanced detection (Fig. 3I). GIANI detected the correct number of cells in 93.7% of cases when using advanced detection. Nuclear localisation errors also generally increased with increased cell density and decreasing signal-to-noise ratio (Fig. 3D,G). The interquartile range (IQR) of nuclear localisation errors was 654–788 nm using basic nuclear detection and 639–674 nm for advanced nuclear detection (Fig. 3J). The cell centroid localisation error was similar for both basic and advanced nuclear detection, with IQRs of 1.87–2.61 μm and 1.78–2.56 μm for basic and advanced detection, respectively (Fig. 3E,H,K).

To benchmark GIANI against other available software, we analysed the same simulated embryos using Imaris (Fig. S1). We found that while Imaris produced a lower nuclear localisation error (IQR was 423–519 nm; Fig. S1F), it miscounted the number of cells in each embryo (38.1% of embryos) far more often than GIANI did (6.3%; Fig. S1E). We also performed a limited evaluation of CellProfiler on a subset of the same simulated data, which resulted in errors larger than those produced by GIANI (Fig. S2) – the nuclear localisation error was 776–786 nm and cell localisation error was 52.3–55.0 μm .

Analysis of mouse embryos

We subsequently applied GIANI to the analysis of two populations of mouse preimplantation embryos at the morula stage (3 to 3.25 days post fertilisation), one control ($n=18$) and one treated with a small-molecule inhibitor (Gerri et al., 2020) ($n=20$). At this stage, two distinct cell populations are discernible – inner and outer cells. In subsequent cell divisions, a blastocyst is formed, whereby the inner cells give rise to an inner cell mass (ICM), and the outer cells become the trophectoderm (TE), a polarized epithelium that will form fetal components of the placenta (Cockburn and Rossant, 2010).

At the morula stage, inner and outer cells display different polarisation states, which influence their cell fate acquisition. The outer cells acquire an apical domain, enriched with the atypical protein kinase C (aPKC) (Plusa et al., 2005). In the polar outer cells, aPKC prevents activation of downstream Hippo pathway kinases, large tumour suppressor kinases 1 and 2 (LATS1/2) (Hirate et al., 2013). Consequently, in outer cells, YAP1 accumulates in the nucleus, where it promotes the expression of GATA3 (Ralston et al., 2010). In contrast, in the apolar inner cells, the activation of the Hippo pathway results in YAP1 cytoplasmic retention, thus maintaining the inner cells in an unspecified state (Cockburn et al., 2013; Frum et al., 2018; Hirate et al., 2013).

We therefore divided cells within each embryo into an ‘inner’ and ‘outer’ population (Fig. 4A,B). This division is based on the distance of the detected nuclear centroid from the embryo centroid.

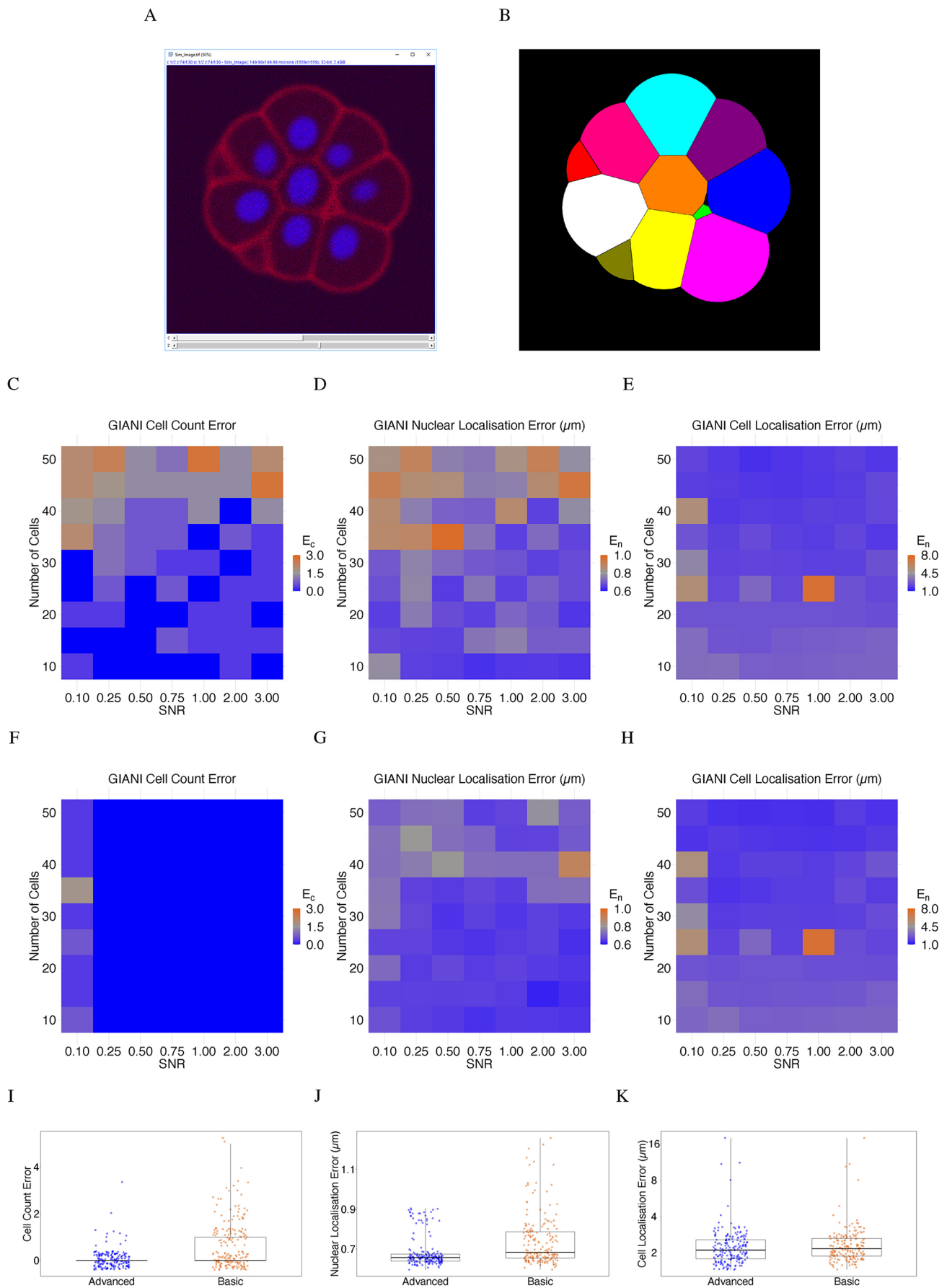


Fig. 3. See next page for legend.

Fig. 3. Validation of GIANI using simulated embryo data. In each of the heat maps, a single tile represents the average of three simulated embryos. The GIANI settings used to produce this data are available to download from <https://doi.org/10.5281/zenodo.6205979>. (A) A 2D slice of an exemplar 3D simulated embryo. (B) The ground truth segmentation of 'A'. (C–H) Absolute errors in cell counts (Ec, calculated according to Eqn 3), nuclear centroid localisation error (Enl) and cell centroid localisation error (Ecl) produced by GIANI for simulated embryos with the indicated number of cells and signal-to-noise ratios (SNRs). Results were obtained using either GIANI's basic (C–E) or advanced (F–H) nuclear detector. (I–K) Comparison of the overall distribution of errors in cell counts, nuclear centroid localisation and cell centroid localisation for GIANI's basic and advanced nuclear detectors, across all SNRs and cell numbers. Each dot represents a single simulated embryo. Box plots show the median (line) and IQR, with the whiskers extending 1.5 times the IQR from the 25th and 75th percentiles

A cell was classified as 'inner' if the following condition held true:

$$\frac{D_i}{D_m} < D_T, \quad (2)$$

where D_i is the Euclidean distance of cell i from the embryo centroid, D_m is the maximum Euclidean distance from any cell in the same embryo to the embryo centroid and D_T is an arbitrarily set distance threshold. For the purposes of this study, we chose a value of 0.5 for D_T – it was found that modifying this value slightly ($\pm 10\%$) did not significantly impact the results (data not shown). The embryo centroid was calculated as the average of all nuclear centroids.

GIANI shows differences in cell morphology and YAP1 and GATA3 expression within inner and outer cells in control embryos

We then applied GIANI to detect variations in morphology and protein expression in mouse preimplantation embryos. We began with a morphological analysis of cells in control embryos. No significant difference was found between median nuclear volumes in inner and outer cell populations (Fig. 4C; $P=0.861$, Wilcoxon rank sum test). A difference in median cell volume between the two populations was also identified, but it was not statistically significant (Fig. 4D; $P=0.069$). However, a comparison of cell-to-nucleus volume ratios revealed a significant difference between median values, with outer cells having a proportionately greater cytoplasmic volume than inner cells (Fig. 4E; $P<0.001$). We also confirmed previous analysis of YAP1 translocation (Nishioka et al., 2009), illustrating that nuclear localisation is significantly higher in outer versus inner cells (Fig. 4F; $P<0.001$). Similarly, GATA3 expression was shown to be higher in outer compared to inner cells (Fig. 4G; $P<0.0001$).

GIANI reveals differences in YAP1 and GATA3 expression in mouse embryos after pharmacological treatment

To further demonstrate the utility of GIANI, we sought to analyse GATA3 and YAP1 expression after treating mouse embryos with a small-molecular inhibitor against aPKC, the upstream regulator of YAP1 and GATA3. The aPKC inhibitor, CRT0276121, has previously been confirmed to specifically inhibit aPKC in various biological and cellular contexts (Aguilar-Aragon et al., 2018; Kjær et al., 2013; Rodriguez et al., 2017). Specifically, in mouse preimplantation embryos, aPKC inhibition has been recently shown to efficiently abrogate YAP1 and GATA3 expression in outer cells (Gerri et al., 2020).

Expression of GATA3 in the nucleus (normalised to DAPI intensity to correct for diminished signal intensity with increasing sample depth) was found to be similarly low in the inner cells of

both control and treated embryos (Fig. 4G; $P=0.841$). However, GATA3 expression in outer cells was found to be significantly lower in the treated embryos relative to the control group ($P<0.002$). Normalised expression of GATA3 was also found to be significantly higher in outer cells of control embryos relative to their inner cells ($P<0.001$), while the same was not true of treated embryos ($P=0.171$). In addition, differences in distribution are evident between control and treated embryos, with two distinct populations evident in both inner and outer cells in control populations (Fig. 4G).

Although no statistically significant difference in nuclear YAP1 expression (normalised to cytoplasmic expression) between control and treated cells were observed when comparing inner cells (Fig. 4H; $P=0.609$), a large difference was observed in outer cells ($P<0.0001$). Moreover, the nuclear/cytoplasmic YAP1 expression ratio was still higher in the outer cells of treated embryos versus inner ($P<0.0001$). Altogether, this demonstrates that GIANI allows for the automated quantification of expression differences between cells following perturbation.

Analysis of blastocysts

To illustrate that GIANI can be run successfully on later stage mouse embryos, we analysed two examples of blastocysts (mouse embryos just prior to implantation, ~4 days post fertilisation) and compared with results from Imaris. A qualitative assessment (in the absence of ground truth segmentations) shows that the results produced by GIANI are comparable to those obtained using Imaris (Fig. S3).

Analysis of larger datasets

Analysis of a large simulated dataset

To test GIANI's ability to handle more complex datasets, we generated a large simulated volume consisting of ~2000 nuclei (available to download from <https://dx.doi.org/10.5281/zenodo.5270244>). We compared the segmentations generated by GIANI with those generated by Imaris (Fig. 5). A qualitative assessment shows that although both software successfully segment the vast majority of cells, errors are apparent, particularly in cases where nuclei are highly clustered (Fig. 5A). We attempted to quantify these segmentation errors using a number of different metrics.

We first compared the distribution of localisation errors produced by GIANI and Imaris (Fig. 5B). Although in both cases nuclei were localised to within ~1 μm or less of their true locations most of the time, the localisation errors produced by Imaris were, overall, marginally lower. But, Imaris had a greater tendency to produce outliers (localisation errors above ~2 μm).

We next looked for any link between localisation error and nuclear density. To do so, we examined the relationship between the localisation error for each successfully detected nucleus and the distance between that nucleus and its nearest neighbour (calculated as the distance between nuclear centroids; Fig. 5C). Although the relationship between these two variables is highly non-linear, it is apparent that, for both GIANI and Imaris, a trend exists – localisation error increases as the distance between nuclei decreases.

Finally, we compared the ability of GIANI and Imaris to successfully detect the simulated nuclei and investigated whether nuclear density influenced the likelihood of successful nuclear detection (Fig. 5D). We found that although both GIANI and Imaris successfully detected the vast majority of nuclei, the sensitivity (percentage of nuclei detected) was slightly higher for GIANI (93.3% vs 89.0%). There was also a clear relationship between inter-nuclear distance and likelihood of successful detection. Of the 85 nuclei that both Imaris and GIANI failed to detect, 95% were 10 μm

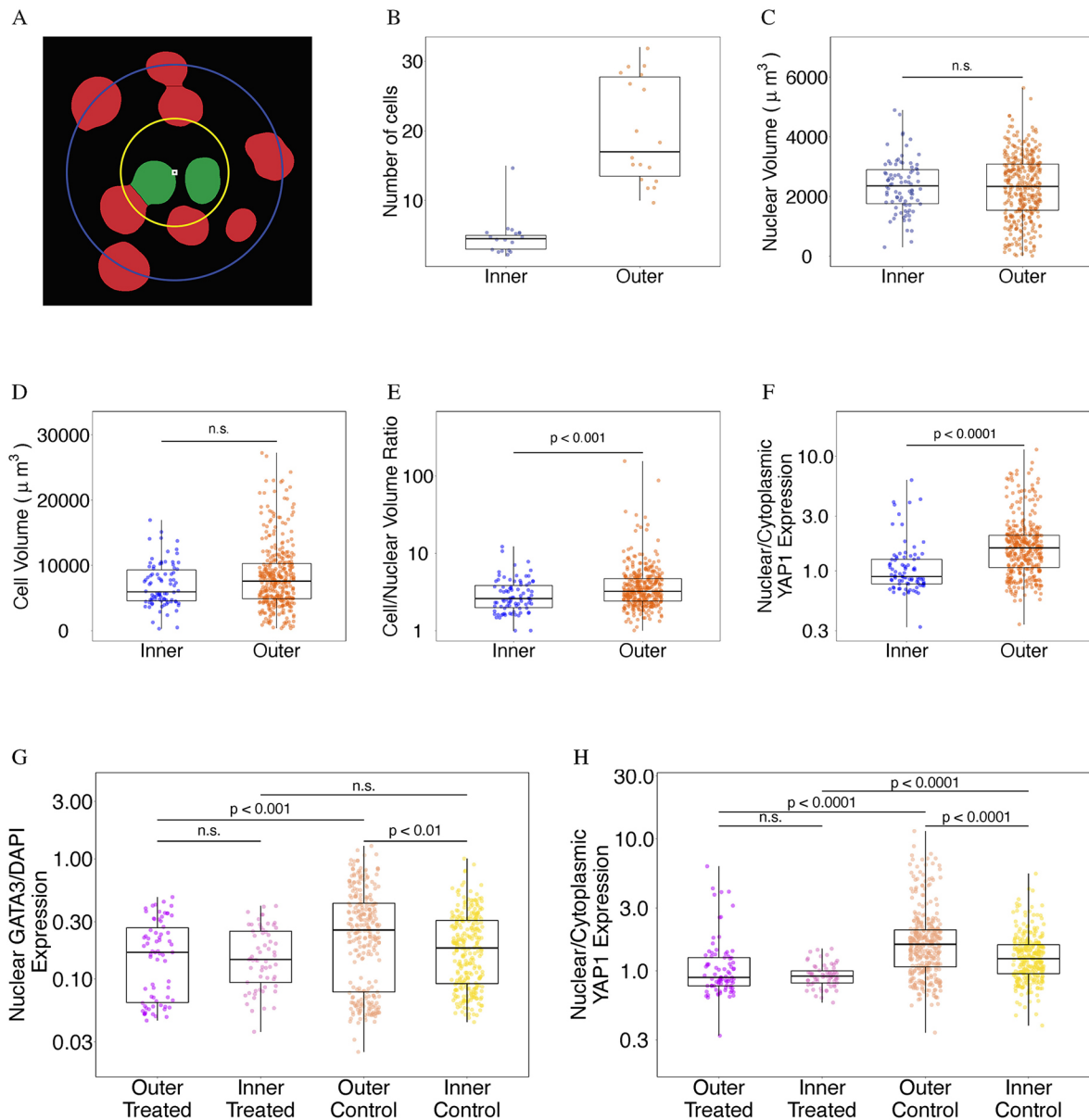


Fig. 4. GIANI reveals differences in morphology and protein expression in mouse embryos. Unless otherwise stated, each dot represents a single cell. The GIANI settings used to produce this data are available to download from <https://doi.org/10.5281/zenodo.6206008>. (A) Illustration of the division of embryo cells into 'outer' (red) and 'inner' (green) subpopulations. The embryo centroid is indicated by the white square. The blue circle has radius D_m and indicates the distance from the embryo centroid to the most distant nucleus. The radius of the yellow circle is $D_T \times D_m$. (B) The number of cells in each embryo divided into outer and inner sub-populations using a value of 0.5 for D_T in control embryos. Each dot represents a single embryo ($n_{\text{control}}=18$). (C) Volume of nuclei in inner and outer populations in control embryos. (D) Volume of cells in inner and outer populations in control embryos. (E) Ratio of cell-to-nuclear volume in inner and outer cells in control embryos. (F) Nuclear/cytoplasmic ratio of YAP1 expression in control embryos. (G) Difference in expression profiles of nuclear GATA3 expression, normalised to DAPI, in control and treated embryos ($n_{\text{treated}}=20$). (H) Difference in nuclear/cytoplasmic ratio of YAP1 expression in control and treated embryos. Box plots show the median (line) and IQR, with the whiskers extending 1.5 times the IQR from the 25th and 75th percentiles. n.s., not significant (two-sample Wilcoxon tests).

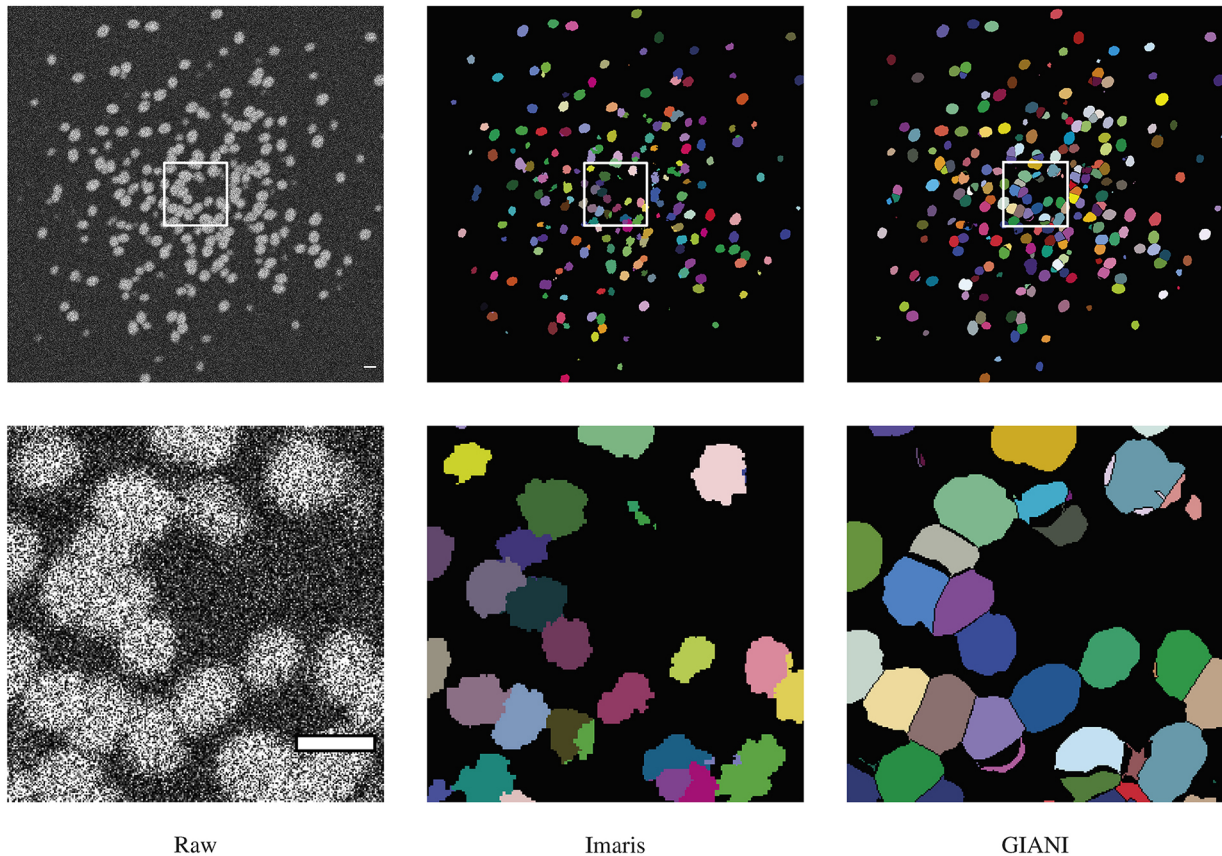
or less from their nearest neighbour. Given that the longest dimension of the simulated nuclei is $\sim 10 \mu\text{m}$, two nuclei that are less than $10 \mu\text{m}$ apart at their centres are likely to significantly overlap. This suggests that a nuclear density of less than approximately $\frac{1}{x^3} \mu\text{m}^{-3}$, where x is the longest dimension of the nuclei, is necessary for reliable segmentation using GIANI.

Analysis of a dataset derived from light-sheet microscopy

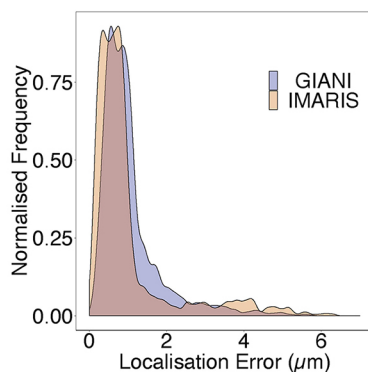
To further emphasise the capacity of GIANI to analyse large volumes of data, we tested it on a *Tribolium castaneum*

embryo dataset derived from light-sheet microscopy (available to download from <https://dx.doi.org/10.5281/zenodo.5270323>), again benchmarking against Imaris (Fig. 6). We obtained this data from the Cell Tracking Challenge (Ulman et al., 2017) and, unfortunately, the ground truth data available is very limited (annotations for only three cells is provided). However, the intention here is to demonstrate that GIANI is capable of segmenting large numbers of nuclei in such data (~ 5600 were detected) and the results are comparable to those obtained using market-leading commercial software (Imaris).

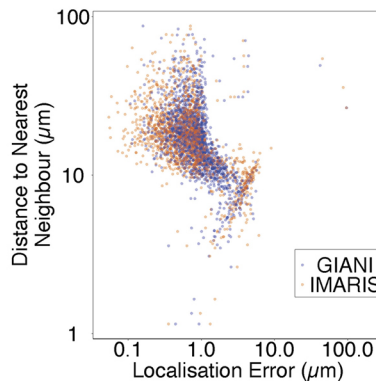
A



B



C



D

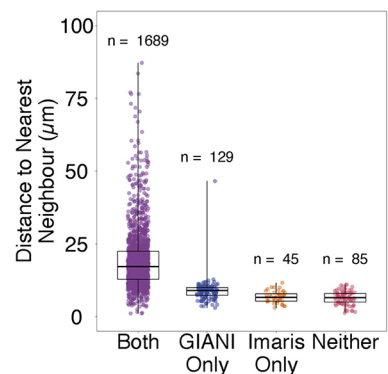


Fig. 5. Demonstration of GIANI with a large simulated dataset. The GIANI and Imaris settings used to produce this data are available to download from <https://doi.org/10.5281/zenodo.6206022>. (A) Illustration of the segmentations produced by GIANI and Imaris on a large simulated dataset (available to download from <https://doi.org/10.5281/zenodo.5270244>). The top row shows a single slice of each 3D volume, whereas the bottom row shows the magnified views of the boxes in the top row images. Scale bars: 20 μm . (B) Distribution of localisation errors produced by both Imaris and GIANI in detecting the simulated nuclei. (C) Relationship between localisation error for detected nuclei and the distance of each nucleus to its nearest neighbour. (D) Influence of distance of nuclei to their nearest neighbour on successful detection. Box plots show the median (line) and IQR, with the whiskers extending 1.5 times the IQR from the 25th and 75th percentiles.

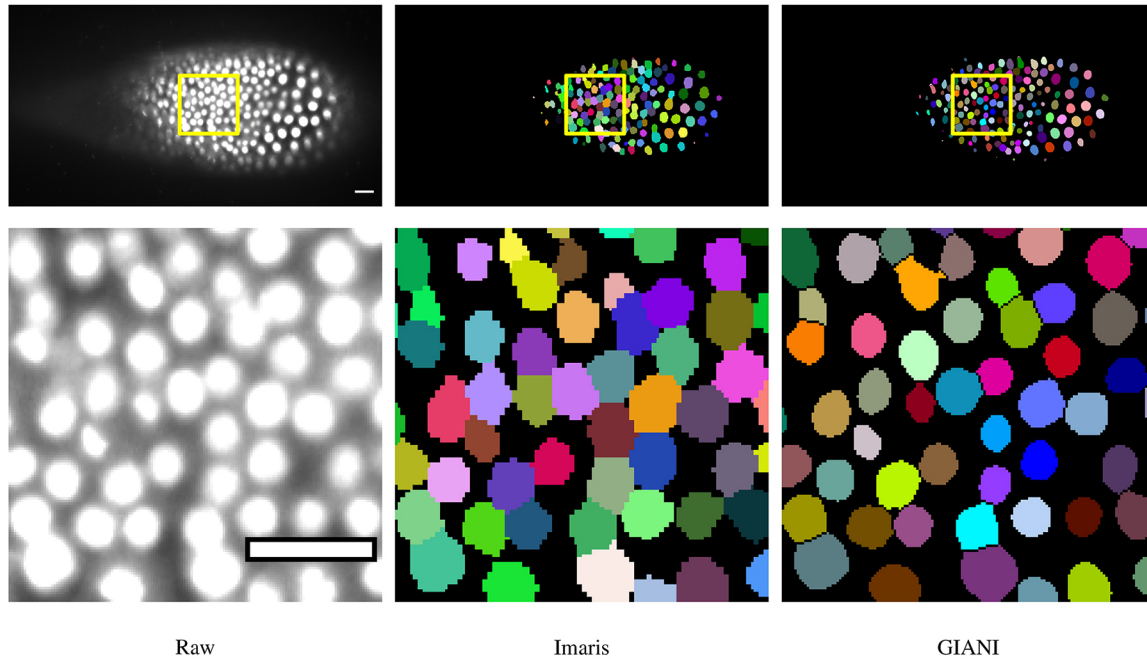
DISCUSSION

Alternative algorithms for nuclei detection

The accurate quantitative analysis of a multicellular image dataset, such as an embryo, is dependent on the correct identification and segmentation of nuclei. While GIANI presently employs generic blob detectors for this purpose, which is similar to other previously-described methods (Lou et al., 2014), other approaches could be

incorporated (Blin et al., 2019; Caicedo et al., 2019; Kostyrykin et al., 2019; Weigert et al., 2020; Yang et al., 2020). In particular, the ability to load pre-trained neural networks, by leveraging DeepImageJ (Gómez-de-Mariscal et al., 2021), for example, or machine-learning classifiers trained with, for example, Weka (Arganda-Carreras et al., 2017) or Ilastik (Berg et al., 2019), may be added in a future release. However, it is already possible for Java

A



B

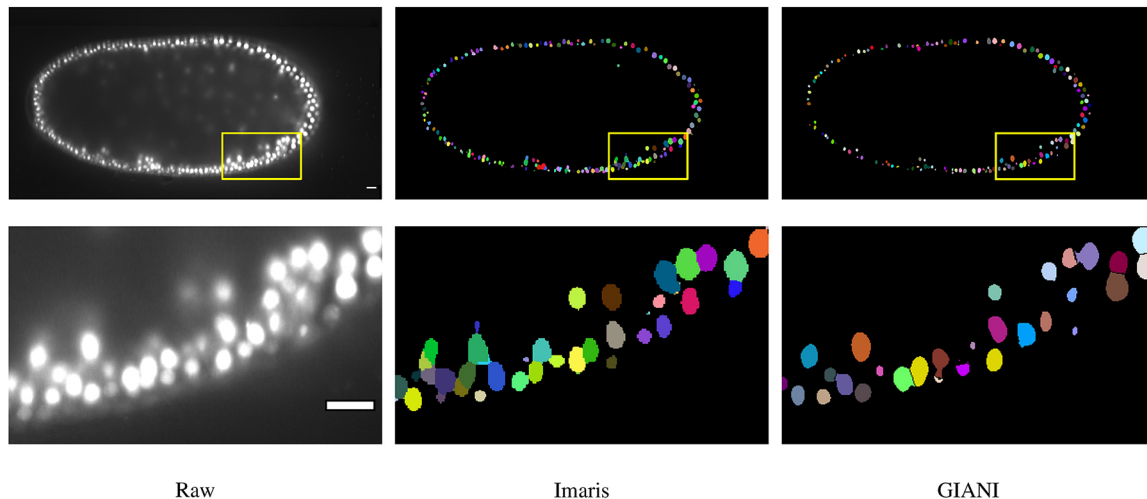


Fig. 6. Demonstration of GIANI on a large light-sheet microscopy dataset. Illustrations of the segmentations produced by GIANI and Imaris on a *Tribolium castaneum* embryo dataset derived from light-sheet microscopy (available to download from <https://doi.org/10.5281/zenodo.5270323>). Two different slices of the 3D volumes are shown, at ~46 μm (A) and ~247 μm (B), to illustrate the variation in nuclei morphologies at different depths. In each case, the top row shows the relevant slice of each 3D volume, whereas the bottom row shows the magnified views of the boxes in the top row images. ~5600 nuclei were detected in the full volume. Scale bars: 20 μm . The GIANI and Imaris settings used to produce this data are available to download from <https://doi.org/10.5281/zenodo.6206042>.

developers to customise and extend GIANI – a template for doing so is provided online (<https://github.com/djpbarr/Giani/wiki>).

Alternative thresholding strategies

One of the challenges associated with the imaging of 3D samples is that slices deeper within the sample will be more prone to scattering effects and therefore exhibit lower intensity. We modelled this process in the generation of our simulated embryos – the simulation process took into consideration depth of slices within a sample when modelling fluorescence intensity. Finding a single global thresholding strategy that does not under-segment the dimmer

cells while also not over-segmenting the brighter cells is challenging.

There are strategies that could be employed to mitigate against these factors. For example, some form of adaptive thresholding, whereby the intensity threshold changes according to z-location, could be used. However, while an optimal adaptive thresholding strategy could be found for a given dataset (such as the simulated data used in this study), implementing a universally-applicable strategy would be difficult. One of the principal design aims of GIANI was simplicity of use, which does not allow for the incorporation of a variety of case-specific segmentation approaches.

Future developments

Given the ongoing interest in studying cells in 'native' 3D extracellular environments (Yamada and Sixt, 2019), future extension to the capabilities of GIANI will include the ability to analyse time-lapse data, as there is currently a lack of open source tools for the quantification of 3D cell migration (Masuzzo et al., 2016). The incorporation of additional functionality from TrackMate [and MaMuT (Wolff et al., 2018) or Mastodon] will be explored to facilitate 3D cell tracking.

Future development will also include the replacement of the 3D ROI Manager interface for visualizing results with a new, custom-built interface. At present, segmented objects are saved solely as FIJI ROI files, but it is intended that support for other formats (such as .stl, .ply, .obj and .x3d) will be added to allow the import of objects into a variety of different software.

More generally, with a view to improving and optimising performance, further use of ImgLib2 (Pietzsch et al., 2012) will be incorporated in future releases. Taking advantage of GPU acceleration is also an aim, most likely by exploiting CLIJ (Haase et al., 2020). At present, the analysis of a single simulated embryo used in this study (approx. 2.1 GB) takes between approximately 30 and 60 min, depending on the number of CPUs available (Fig. S4).

Conclusion

We have used GIANI to quantitatively analyse mouse embryos in 3D. This analysis has revealed differences in morphology and protein expression between different experimental conditions. Analysis of simulated ground truth data was used to confirm the validity of these results. Further development of GIANI is planned, with the specific aim of improving segmentations in noisy and dense fields of view, common in 3D images of cells. Extension to timelapse analysis is also planned. GIANI is freely available on GitHub (<https://github.com/djpbarry/Giani>) and we anticipate that it will be a useful resource for the community to perform routine, automated quantification of complex imaging data.

MATERIALS AND METHODS

Simulated data generation

Simulated data sets were generated using an extension of a previously described method (Rajasekaran et al., 2016). Simulated nuclei (ellipsoidal with axis dimensions of $\sim 10.0 \times 7.5 \times 7.5 \mu\text{m}$) were positioned as previously described (Rajasekaran et al., 2016), then cell membranes were approximated using a Euclidean Distance Map constructed around nuclei. The simulated images were then convolved with a Gaussian point-spread function, sub-sampled and noise added from a gamma distribution. The complete code for simulated image generation is available on GitHub (<https://github.com/djpbarry/Embryo-Generator>).

Metrics for segmentation quality assessment

We calculated the cell count error (E_c) as:

$$E_c = |N_g - N_{gr}|, \quad (3)$$

where N_{gr} is the actual number of cells present in a simulated embryo and N_g is the number counted by GIANI. Nuclear (E_{nl}) and cell (E_{cl}) centroid localisation errors were calculated based on the Euclidean distance between the known ground truth centroids and the centroids of the segmentations produced by GIANI.

Mouse zygote collection

Four- to eight-week-old (C57BL6×CBA) F1 female mice were super-ovulated using injection of 5 IU of pregnant mare serum gonadotrophin (PMSG; Sigma-Aldrich). At 48 h after PMSG injection, 5 IU of human chorionic gonadotrophin (HCG; Sigma-Aldrich) was administered. Superovulated females were set up for mating with eight-week-old or

older (C57BL6×CBA) F1 males. Mice were maintained on a 12 h light–12 h dark cycle. Mouse zygotes were isolated in EmbryoMax FHM mouse embryo medium (Sigma-Aldrich; MR-122-D) under mineral oil (Origio; ART-4008-5P) and cumulus cells were removed with hyaluronidase (Sigma-Aldrich; H4272). All animal research was performed in compliance with the UK Home Office Licence Number 70/8560.

Mouse embryo culture

Mouse embryos were cultured in drops of pre-equilibrated Global medium (LifeGlobal; LGGG-20) supplemented with 5 mg/ml protein supplement (LifeGlobal; LGPS-605) and overlaid with mineral oil (Origio; ART-4008-5P). Preimplantation embryos were incubated at 37°C and 5.5% CO₂ and cultured up to the day of analysis.

Inhibitor treatment

Inhibitor experiment was performed as previously described (Gerri et al., 2020). Briefly, the aPKC inhibitor CRT0276121 (Cancer Research Technology) was dissolved in DMSO to 10 mM stock concentration and diluted to the optimal concentration of 8 μM in pre-equilibrated embryo culture medium. Mouse embryos were incubated in pre-equilibrated medium with 8 μM of CRT0276121 from four-cell to morula stage (3 to 3.25 days post-fertilisation). Control mouse embryos were developed in pre-equilibrated medium where volume-matched DMSO was added.

Immunofluorescence

Embryos were fixed with freshly prepared 4% paraformaldehyde in PBS that was pre-chilled at 4°C. Embryo fixation was performed for 20 min at room temperature (RT) and then the embryos were transferred through three washes of 1× PBS with 0.1% Tween-20 to remove residual paraformaldehyde. Embryos were permeabilized with 1× PBS with 0.5% Triton X-100 and then blocked in blocking solution (3% BSA in 1× PBS with 0.2% Triton X-100) for 2 h at RT on a rotating shaker. Then, embryos were incubated with primary antibodies (listed in Table S1) diluted in blocking solution overnight at 4°C on rotating shaker.

The following day, embryos were washed in 1× PBS with 0.2% Triton X-100 for 20 min at RT on a rotating shaker and then incubated with secondary antibodies diluted in blocking solution for 1 h at RT on a rotating shaker in the dark. Next, embryos were washed in 1× PBS with 0.2% Triton X-100 for 20 min at RT on rotating shaker. Finally, embryos were placed in 1× PBS with 0.1% Tween-20 with Vectashield with DAPI mounting medium (Vector Lab; H-1200) (1:30 dilution). Embryos were placed on μ -Slide 8-well dishes (Ibidi; 80826) for confocal imaging.

Image acquisition

All images were acquired on a Leica SP5 laser scanning confocal microscope using a Leica 1.3 NA 63× HCX PL APO CS glycerol objective and a voxel size of approximately $0.1 \times 0.1 \times 1.0 \mu\text{m}$ in x, y and z, respectively.

Statistical analysis

All statistical analyses in this study were performed using RStudio (<https://www.rstudio.com>). The tests performed in this paper are two-sample Wilcoxon tests (also known as Mann–Whitney) (Mann and Whitney, 1947); no assumptions are made regarding the nature of data distribution. All box plots show the median and inter-quartile range, with the whiskers extending 1.5 times the interquartile range from the 25th and 75th percentiles. Unless otherwise stated, each dot in dot plots represents a single cell.

Acknowledgements

Thanks to Kurt Anderson for his constructive comments on the manuscript.

Competing interests

The authors declare no competing or financial interests.

Author contributions

Conceptualization: D.J.B., C.G.; Methodology: D.J.B., C.G., D.M.B., R.D.; Software: D.J.B.; Validation: D.J.B., C.G.; Formal analysis: D.J.B., C.G.; Investigation: D.J.B., C.G.; Data curation: C.G., D.M.B., R.D.; Writing - original draft: D.J.B.; Writing - review & editing: C.G., K.K.N.

Funding

This work was supported by the Francis Crick Institute, which receives its core funding from Cancer Research UK (FC001120, FC001999), the UK Medical Research Council (FC001120, FC001999) and the Wellcome Trust (FC001120, FC001999). Open Access funding provided by The Francis Crick Institute. Deposited in PMC for immediate release.

Data availability

All experimental and simulated datasets used in this study are available to download from the BioImage Archive (accession numbers S-BIAD328 and S-BIAD334). Links to all other data files are listed in supplemental information.

Peer review history

The peer review history is available online at <https://journals.biologists.com/jcs/article-lookup/doi/10.1242/jcs.259511>.

References

Aguilar-Aragon, M., Elbediwy, A., Foglizzo, V., Fletcher, G. C., Li, V. S. W. and Thompson, B. J. (2018). Pak1 kinase maintains apical membrane identity in epithelia. *Cell Rep.* **22**, 1639–1646. doi:10.1016/j.celrep.2018.01.060

Arganda-Carreras, I., Kaynig, V., Rueden, C., Eliceiri, K. W., Schindelin, J., Cardona, A. and Sebastian Seung, H. (2017). Trainable Weka segmentation: a machine learning tool for microscopy pixel classification. *Bioinformatics* **33**, 2424–2426. doi:10.1093/bioinformatics/btx180

Berg, S., Kutra, D., Kroeger, T., Straehle, C. N., Kausler, B. X., Haubold, C., Schiegg, M., Ales, J., Beier, T., Rudy, M. et al. (2019). ilastik: interactive machine learning for (bio)image analysis. *Nat. Methods* **16**, 1226–1232. doi:10.1038/s41592-019-0582-9

Blin, G., Sadurska, D., Portero Migueles, R., Chen, N., Watson, J. A. and Lowell, S. (2019). Nessys: a new set of tools for the automated detection of nuclei within intact tissues and dense 3D cultures. *PLoS Biol.* **17**, e3000388. doi:10.1371/journal.pbio.3000388

Caicedo, J. C., Goodman, A., Karhohs, K. W., Cimini, B. A., Ackerman, J., Haghighi, M., Heng, C., Becker, T., Doan, M., McQuin, C. et al. (2019). Nucleus segmentation across imaging experiments: the 2018 Data Science Bowl. *Nat. Methods* **16**, 1247–1253. doi:10.1038/s41592-019-0612-7

Cautun, M., van de Weygaert, R. and Jones, B. J. T. (2012). NEXUS: tracing the cosmic web connection. *Mon. Not. R. Astron. Soc.* **429**, 1286–1308. doi:10.1093/mnras/sts416

Cockburn, K. and Rossant, J. (2010). Making the blastocyst: lessons from the mouse. *J. Clin. Invest.* **120**, 995–1003. doi:10.1172/JCI41229

Cockburn, K., Biechele, S., Garner, J. and Rossant, J. (2013). The Hippo pathway member Nf2 is required for inner cell mass specification. *Curr. Biol.* **23**, 1195–1201. doi:10.1016/j.cub.2013.05.044

de Chaumont, F., Dallongeville, S., Chenouard, N., Hervé, N., Pop, S., Provoost, T., Meas-Yedid, V., Pankajakshan, P., Lecomte, T., Le Montagner, Y. et al. (2012). Icy: an open bioimage informatics platform for extended reproducible research. *Nat. Methods* **9**, 690–696. doi:10.1038/nmeth.2075

Duval, K., Grover, H., Han, L.-H., Mou, Y., Pegoraro, A. F., Fredberg, J. and Chen, Z. (2017). Modeling physiological events in 2D vs. 3D cell culture. *Physiology* **32**, 266–277. doi:10.1152/physiol.00036.2016

Frum, T., Murphy, T. M. and Ralston, A. (2018). HIPPO signaling resolves embryonic cell fate conflicts during establishment of pluripotency in vivo. *eLife* **7**, e42298. doi:10.7554/eLife.42298

Gerri, C., McCarthy, A., Alanis-Lobato, G., Demtschenko, A., Bruneau, A., Loubersac, S., Fogarty, N. M. E., Hampshire, D., Elder, K., Snell, P. et al. (2020). Initiation of a conserved trophoblast program in human, cow and mouse embryos. *Nature* **587**, 443–447. doi:10.1038/s41586-020-2759-x

Gómez-de-Mariscal, E., García-López-de-Haro, C., Ouyang, W., Donati, L., Lundberg, E., Unser, M., Muñoz-Barrutia, A. and Sage, D. (2021). DeepImageJ: a user-friendly environment to run deep learning models in ImageJ. *Nat. Methods* **18**, 1192–1195. doi:10.1038/s41592-021-01262-9

Haase, R., Royer, L. A., Steinbach, P., Schmidt, D., Dibrov, A., Schmidt, U., Weigert, M., Maghelli, N., Tomancak, P., Jug, F. et al. (2020). CLN: GPU-accelerated image processing for everyone. *Nat. Methods* **17**, 5–6. doi:10.1038/s41592-019-0650-1

Hirate, Y., Hirahara, S., Inoue, K., Suzuki, A., Alarcon, V. B., Akimoto, K., Hirai, T., Hara, T., Adachi, M., Chida, K. et al. (2013). Polarity-dependent distribution of angiotensin II localizes Hippo signaling in preimplantation embryos. *Curr. Biol.* **23**, 1181–1194. doi:10.1016/j.cub.2013.05.014

Jones, T. R., Carpenter, A. and Golland, P. (2005). Voronoi-based segmentation of cells on image manifolds. In *Computer Vision for Biomedical Image Applications* (ed. Y. Liu, T. Jiang and C. Zhang), pp. 535–543. Springer Berlin Heidelberg.

Kjær, S., Linch, M., Purkiss, A., Kostecky, B., Knowles, P. P., Rosse, C., Riou, P., Soudy, C., Kaye, S., Patel, B. et al. (2013). Adenosine-binding motif mimicry and cellular effects of a thieno[2,3- d]pyrimidine-based chemical inhibitor of

atypical protein kinase C isoenzymes. *Biochem. J.* **451**, 329–342. doi:10.1042/BJ20121871

Kostykin, L., Schnörr, C. and Rohr, K. (2019). Globally optimal segmentation of cell nuclei in fluorescence microscopy images using shape and intensity information. *Med. Image Anal.* **58**, 101536–101536. doi:10.1016/j.media.2019.101536

Lamprecht, M. R., Sabatini, D. M. and Carpenter, A. E. (2007). CellProfiler™: free, versatile software for automated biological image analysis. *BioTechniques* **42**, 71–75. doi:10.2144/000112257

Legland, D., Arganda-Carreras, I. and Andrey, P. (2016). MorphoLibJ: integrated library and plugins for mathematical morphology with ImageJ. *Bioinformatics* **32**, 3532–3534. doi:10.1093/bioinformatics/btw413

Linker, M., Rueden, C. T., Allan, C., Burel, J.-M., Moore, W., Patterson, A., Loranger, B., Moore, J., Neves, C., Macdonald, D. et al. (2010). Metadata matters: access to image data in the real world. *J. Cell Biol.* **189**, 777–782. doi:10.1083/jcb.201004104

Lou, X., Kang, M., Xenopoulos, P., Muñoz-Descalzo, S. and Hadjantonakis, A.-K. (2014). A rapid and efficient 2D/3D nuclear segmentation method for analysis of early mouse embryo and stem cell image data. *Stem Cell Rep.* **2**, 382–397. doi:10.1016/j.stemcr.2014.01.010

Mann, H. B. and Whitney, D. R. (1947). On a test of whether one of two random variables is stochastically larger than the other. *Ann. Math. Stat.* **18**, 50–60. doi:10.1214/aoms/1177730491

Masuzzo, P., Van Troys, M., Ampe, C. and Martens, L. (2016). Taking aim at moving targets in computational cell migration. *Trends Cell Biol.* **26**, 88–110. doi:10.1016/j.tcb.2015.09.003

Meijering, E., Carpenter, A. E., Peng, H., Hamprecht, F. A. and Olivo-Marin, J. C. (2016). Imagining the future of bioimage analysis. *Nat. Biotechnol.* **34**, 1250–1255. doi:10.1038/nbt.3722

Nishioka, N., Inoue, K., Adachi, K., Kiyonari, H., Ota, M., Ralston, A., Yabuta, N., Hirahara, S., Stephenson, R. O., Ogonuki, N. et al. (2009). The Hippo signaling pathway components Lats and Yap pattern Tead4 activity to distinguish mouse trophoblast from inner cell mass. *Dev. Cell* **16**, 398–410. doi:10.1016/j.devcel.2009.02.003

Ollion, J., Cochenne, J., Loll, F., Escudé, C. and Boudier, T. (2013). TANGO: a generic tool for high-throughput 3D image analysis for studying nuclear organization. *Bioinformatics* **29**, 1840–1841. doi:10.1093/bioinformatics/btt276

Pietzsch, T., Preibisch, S., Tomancák, P. and Saalfeld, S. (2012). ImgLib2—generic image processing in Java. *Bioinformatics* **28**, 3009–3011. doi:10.1093/bioinformatics/bts543

Plusa, B., Frankenberg, S., Chalmers, A., Hadjantonakis, A. K., Moore, C. A., Papalopulu, N., Papaioannou, V. E., Glover, D. M. and Zernicka-Goetz, M. (2005). Downregulation of Par3 and aPKC function directs cells towards the ICM in the preimplantation mouse embryo. *J. Cell Sci.* **118**, 505–515. doi:10.1242/jcs.01666

Rajasekaran, B., Uriu, K., Valentin, G., Tinevez, J.-Y. and Oates, A. C. (2016). Object segmentation and ground truth in 3D embryonic imaging. *PLoS ONE* **11**, e0150853. doi:10.1371/journal.pone.0150853

Ralston, A., Cox, B. J., Nishioka, N., Sasaki, H., Chea, E., Rugg-Gunn, P., Guo, G., Robson, P., Draper, J. S. and Rossant, J. (2010). Gata3 regulates trophoblast development downstream of Tead4 and in parallel to Cdx2. *Development* **137**, 395–403. doi:10.1242/dev.038828

Rodriguez, J., Peglion, F., Martin, J., Hubatsch, L., Reich, J., Hirani, N., Gubieda, A. G., Roffey, J., Fernandes, A. R., St Johnston, D. et al. (2017). aPKC cycles between functionally distinct PAR protein assemblies to drive cell polarity. *Dev. Cell* **42**, 400–415.e9. doi:10.1016/j.devcel.2017.07.007

Schindelin, J., Arganda-Carreras, I., Frise, E., Kaynig, V., Longair, M., Pietzsch, T., Preibisch, S., Rueden, C., Saalfeld, S., Schmid, B. et al. (2012). Fiji: an open-source platform for biological-image analysis. *Nat. Methods* **9**, 676–682. doi:10.1038/nmeth.2019

Schneider, C. A., Rasband, W. S. and Eliceiri, K. W. (2012). NIH Image to ImageJ: 25 years of image analysis. *Nat. Methods* **9**, 671–675. doi:10.1038/nmeth.2089

Tinevez, J.-Y., Perry, N., Schindelin, J., Hoopes, G. M., Reynolds, G. D., Laplantine, E., Bednarek, S. Y., Shorte, S. L. and Eliceiri, K. W. (2017). TrackMate: an open and extensible platform for single-particle tracking. *Methods* **115**, 80–90. doi:10.1016/j.ymeth.2016.09.016

Tosi, S., Bardia, L., Filgueira, M. J., Calon, A. and Colombelli, J. (2020). LOBSTER: an environment to design bioimage analysis workflows for large and complex fluorescence microscopy data. *Bioinformatics* **36**, 2634–2635. doi:10.1093/bioinformatics/btz945

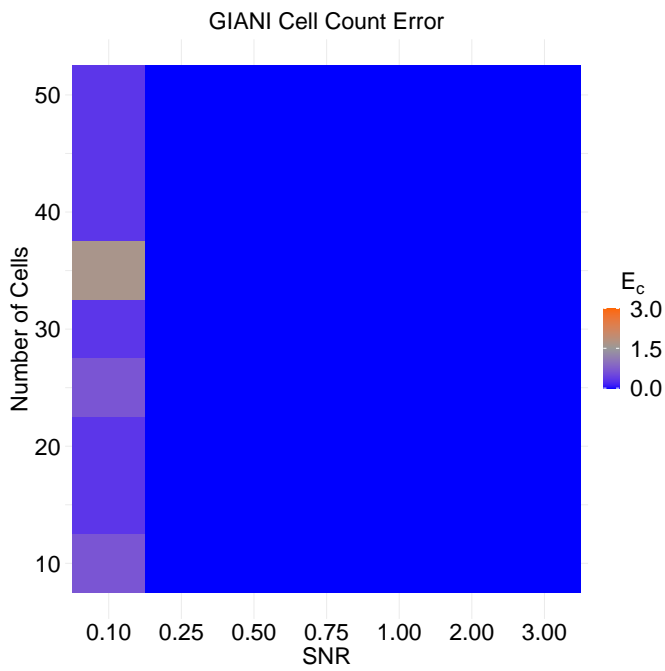
Ulman, V., Maška, M., Magnusson, K. E. G., Ronneberger, O., Haubold, C., Harder, N., Matula, P., Matula, P., Svoboda, D., Radojevic, M. et al. (2017). An objective comparison of cell-tracking algorithms. *Nat. Methods* **14**, 1141–1152. doi:10.1038/nmeth.4473

Weigert, M., Schmidt, U., Haase, R., Sugawara, K. and Myers, G. (2020). Star-convex Polyhedra for 3D object detection and segmentation in microscopy. In *2020 IEEE Winter Conference on Applications of Computer Vision (WACV)*, pp. 3655–3662.

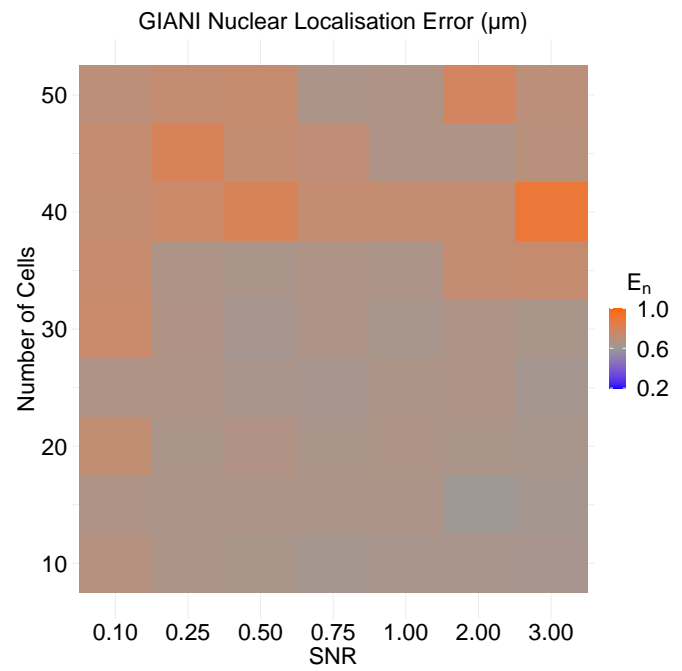
Wolff, C., Tinevez, J.-Y., Pietzsch, T., Stamatakis, E., Harich, B., Guignard, L., Preibisch, S., Shorte, S., Keller, P. J., Tomancak, P. et al. (2018). Multi-view

- light-sheet imaging and tracking with the MaMuT software reveals the cell lineage of a direct developing arthropod limb. *eLife* **7**, e34410. doi:10.7554/eLife.34410
- Yamada, K. M. and Sixt, M.** (2019). Mechanisms of 3D cell migration. *Nat. Rev. Mol. Cell Biol.* **20**, 738-752. doi:10.1038/s41580-019-0172-9
- Yang, L., Ghosh, R. P., Franklin, J. M., Chen, S., You, C., Narayan, R. R., Melcher, M. L. and Liphardt, J. T.** (2020). NuSeT: a deep learning tool for reliably separating and analyzing crowded cells. *PLoS Comput. Biol.* **16**, e1008193. doi:10.1371/journal.pcbi.1008193

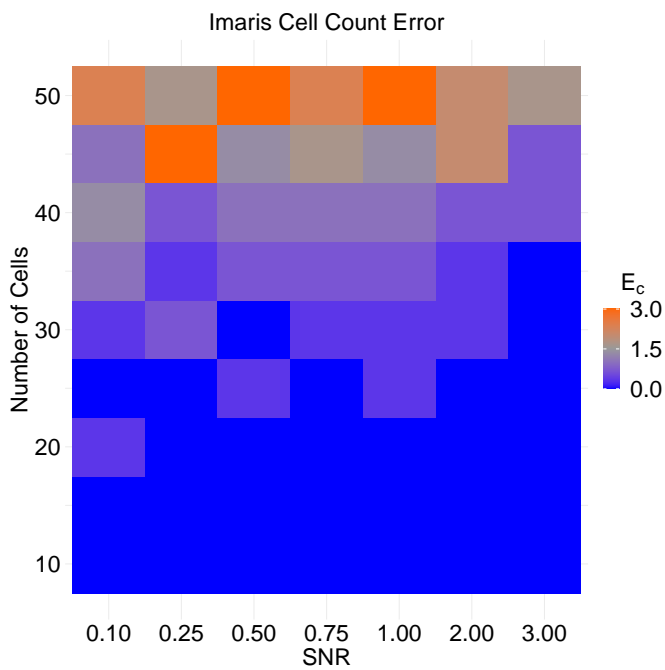
A



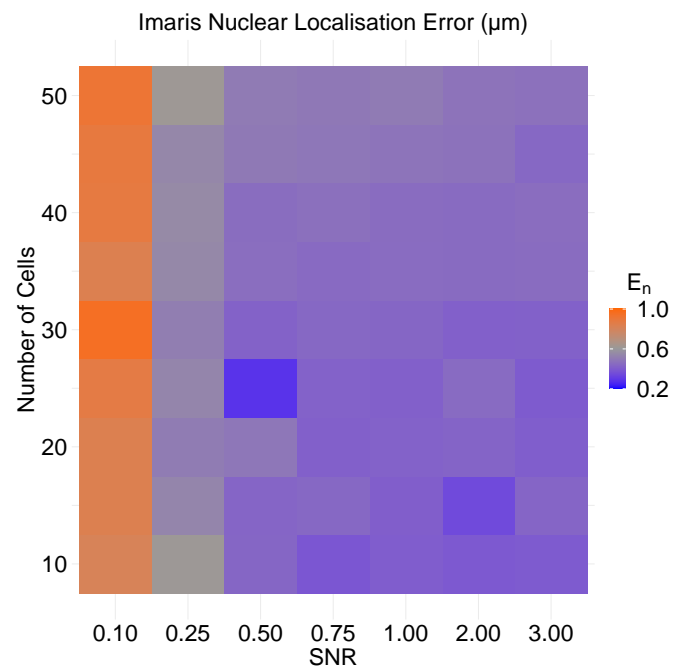
B



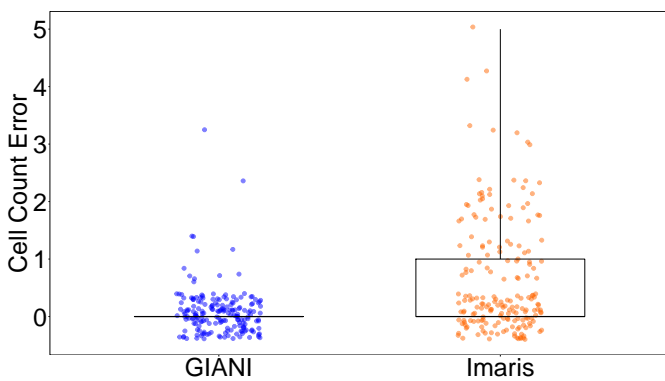
C



D



E



F

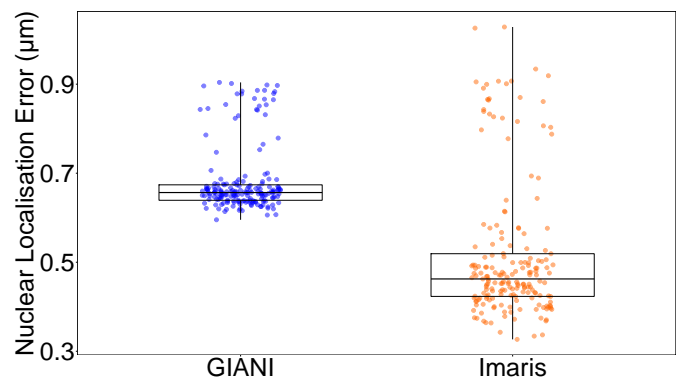


Fig S1. Accuracy of simulated nuclei detection and localisation by GIANI and Imaris.

In each of the heat maps, a single tile represents the average of three simulated embryos. The GIANI and Imaris settings used to produce this data are available to download from <https://doi.org/10.5281/zenodo.6206087>. A: Absolute errors in cell counts (E_C) produced by GIANI for simulated embryos with the indicated number of cells and signal-to-noise ratios (SNR). B: Absolute errors in nuclear centroid localisation (E_{nl}) produced by GIANI. C: Absolute errors in cell counts produced by Imaris. D: Absolute errors in nuclear centroid localisation produced by Imaris. E - F: Comparison of the overall distribution of errors in cell counts and nuclear centroid localisation GIANI and Imaris, across all SNRs and cell numbers. Each dot represents a single simulated embryo.

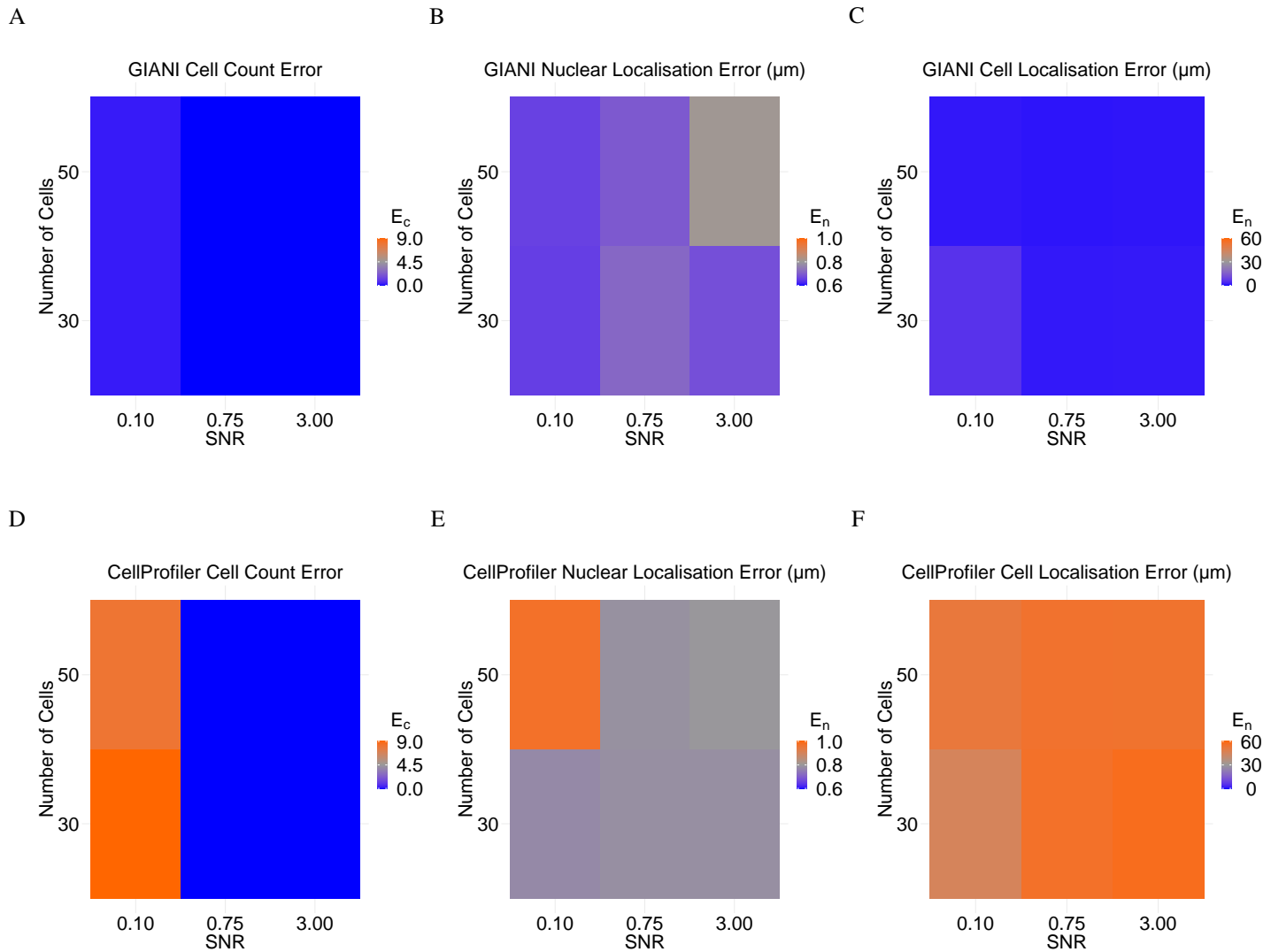


Fig. S2. Accuracy of simulated nuclei and cell detection and localisation by GIANI and CellProfiler compared. The data shown in A - C is a subset of that shown in Fig 3F - H. In D - F, each tile represents a single simulated embryo, which was reduced in size to 512 x 512 x 112 voxels prior to running the pipeline. A: Absolute errors in cell counts (E_c) produced by GIANI for

simulated embryos with the indicated number of cells and signal-to-noise ratios (SNR).

B: Absolute errors in nuclear centroid localisation (E_{nl}) produced by GIANI. C:

Absolute errors in cell centroid localisation error (E_{cl}) produced by GIANI. D:

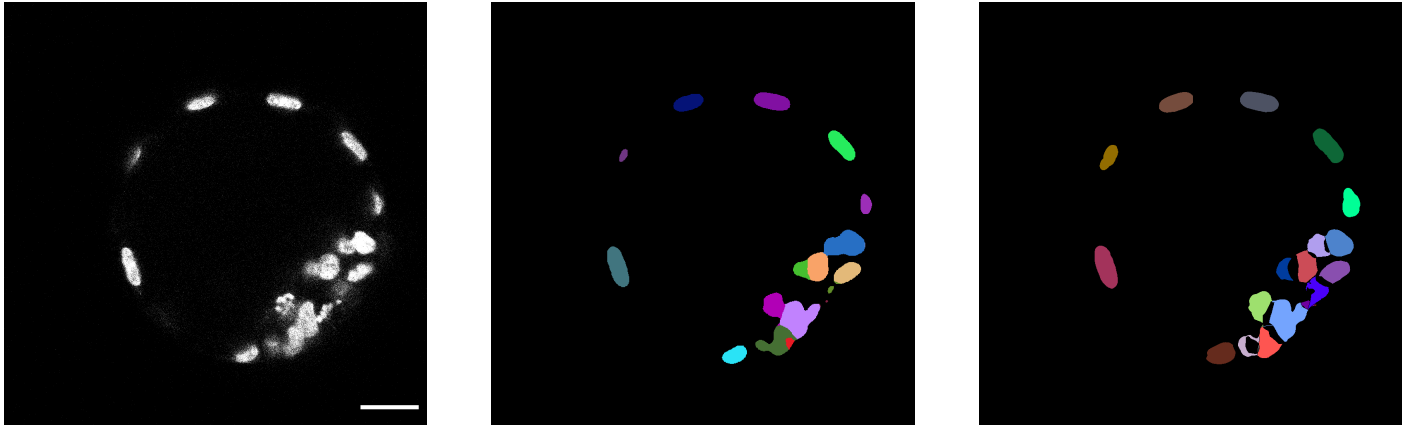
Absolute errors in cell counts produced by CellProfiler. E: Absolute errors in nuclear

centroid localisation produced by CellProfiler. F: Absolute errors in cell centroid

localisation error produced by CellProfiler. The CellProfiler pipeline used and raw data

are available to download from: <https://dx.doi.org/10.5281/zenodo.5286507>.

A



B



Raw

Imaris

GIANI

Fig. S3. Comparison of mouse blastocyst nuclear segmentations between GIANI and Imaris.. A single slice of (A) expanded and (B) hatching blastocysts are shown, together with the segmentations produced by Imaris and GIANI. Scale bars are all equivalent to 20 μm . The GIANI and Imaris settings used to produce this data, together with the raw image data, are available to download from <https://dx.doi.org/10.5281/zenodo.5286670>.

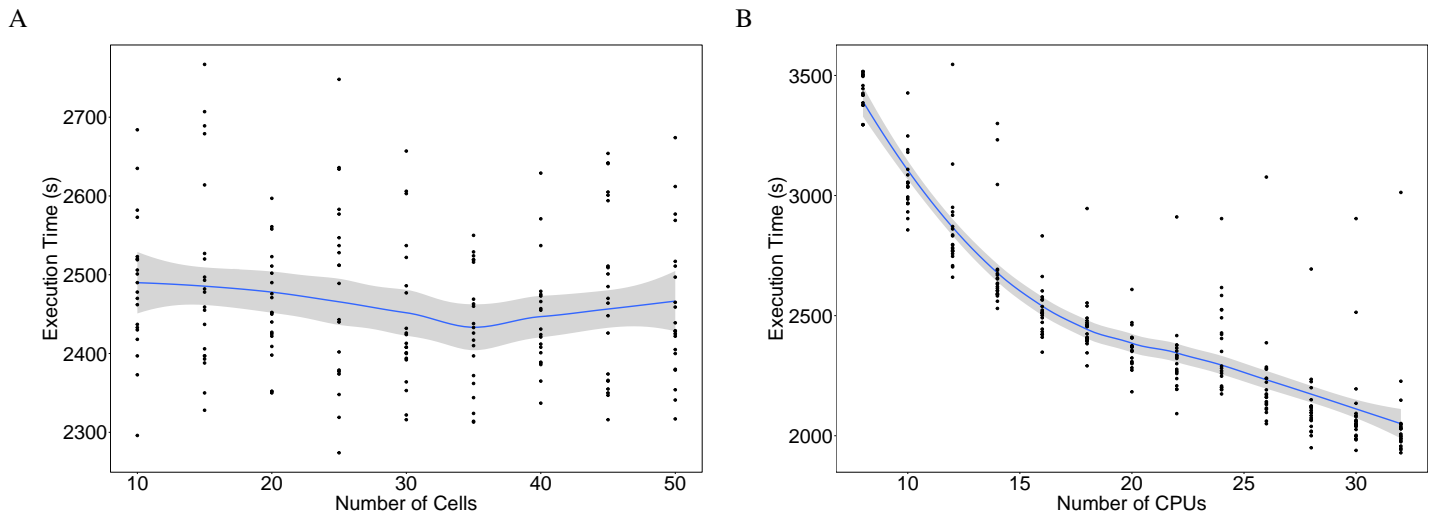


Fig. S4. Execution time of GIANI is independent of cell number, but decreases with increasing CPU availability. A: The length of time taken by GIANI to analyse simulated embryos versus the number of cells in the embryo. Each point represents the execution time for a single embryo - approximately 20 embryos were analysed for each cell number. The blue line represents a moving average calculated with LOESS smoothing. The grey bands represent the 95% confidence interval. B: The length of time taken by GIANI to analyse simulated embryos consisting of 30 cells versus the number of available CPUs. Each point represents the execution time for a single embryo - approximately 20 embryos were analysed for each CPU number. The blue line represents a moving average calculated with LOESS smoothing. The grey bands represent the 95% confidence interval.

Table S1. Primary antibodies used in this study and the dilution at which they were used.

Antibody	Supplier	Catalogue Number	Dilution
YAP1	Abnova	H00010413-M01	1:50
GATA3	R&D	AF2605	1:200
E-CADHERIN	Life Technologies	131900	1:400